



Enhanced electrocatalytic performance on polymer-stabilized graphene decorated with alloy nanoparticles for ethanol oxidation reaction in alkaline media

Abhijit Dutta, Jianyong Ouyang*

Department of Materials Science and Engineering, National University of Singapore, Singapore

ARTICLE INFO

Article history:

Received 6 November 2013

Received in revised form 21 February 2014

Accepted 8 April 2014

Available online 18 April 2014

Keywords:

Electrocatalysis

Graphene

Nanoparticles

Alloy

AuPt

ABSTRACT

We explore a green method to grow metal alloy nanoparticles (NPs) on reduced graphene oxide stabilized with polyvinylpyrrolidone (PVP) in aqueous solution with sodium borohydride as a reducing agent for metal ions. PVP was used to stabilize nano-graphene sheets (NGs) in solution and prevent their aggregation. The synthetic experimental conditions were studied to control the size, shape and distribution of alloy nanoparticles anchored on the graphene sheets. AuPt nanoparticles on PVP-stabilized graphene (PVP-NGs-AuPt) show higher catalytic activity and stability than those on graphene without PVP (NGs-AuPt) toward the ethanol oxidation reaction (EOR) in alkaline media. PVP-NGs-AuPt can increase the EOR peak current density by more than 160%, ~100% and 78% as compared with Pt on carbon, AuPt on carbon and NGs-AuPt, respectively. Moreover, the poisoning of PVP-NGs-AuPt during the EOR is less significant than that of NGs-AuPt, as revealed by analyzing the intermediates products, acetate and carbonate, by ion exchange chromatography. The high electrocatalytic activity of PVP-NGs-AuPt is attributed to the surface activation by OH⁻ and the interaction between the AuPt NPs and graphene, which can improve the CO oxidation within the applied potential range.

© 2014 Elsevier B.V. All rights reserved.

1. Introduction

Direct alcohol fuel cells convert chemical energy into electricity in high energy conversion efficiency. Alcohols have high energy density and are readily available. It is convenient to transport and store alcohols. But there are a couple of challenges to overcome for the commercialization of direct alcohol fuel cells on a large scale. A key issue is to select appropriate electrode–fuel combinations in acidic or alkaline medium [1–3]. The major hurdle for the commercialization of direct alcohol fuel cells lies in using the precious Pt with high loading as the electrocatalyst [2–5]. Although Pt is a very effective catalyst for the oxygen reduction at cathode and the alcohol oxidation at anode [6–8], it is a rare metal and very expensive [4,5]. In addition, the Pt surface can be readily poisoned by adsorbed CO. In order to overcome these issues, Pt nanoparticles (NPs) and its alloy NPs have been investigated as the electrocatalyst of fuel cells. The Pt loading can be lowered and its catalytic activity can be greatly increased by alloying with Au. Because Au is more electronegative than Pt, electrons transfer from Pt atoms

into Au atoms in PtAu alloy. This electron transfer can improve the catalytic activity. In addition, the negatively charged Au atoms can facilitate the oxygen supply, leading to the complete oxidation of ethanol and prohibition of the building up of CO_{ads} on the catalyst surface. Hence, AuPt NPs have been studied as the electrocatalysts for many energy conversion-related chemical reactions, including the low molecular weight alcohol oxidation, formic acid oxidation, formaldehyde oxidation, ethylene glycol oxidation and oxygen reduction [9–19]. It was observed that the AuPt alloy NPs have remarkably higher catalytic activity than Pt. Apart from the alloying effect, the supporter of metal NPs can also significantly affect the electrocatalytic activity [20]. The requirements for the supporter include high surface area, suitable porosity for ion transport and high electrical conductivity. Conventionally, carbon such as Vulcan XC-72 (carbon black, XC-72) is popular as the supporter because of its large surface area, relatively good electrical conductivity and high porosity [21]. But the surface area of carbon blacks is mainly due to the micropores of less than 1 nm. These micropores are difficult to fully access for electrolyte, so that they make little contribution to the catalysis [22]. Graphene has received considerable attention as the replacement of carbon black as the supporter for nanocatalyst [23–34]. It has a theoretical surface area of about 2600 m² g⁻¹ and a high electrical conductivity of 10⁵–10⁶ S m⁻¹. It

* Corresponding author. Tel.: +65 6516 1472; fax: +65 6776 3604.

E-mail addresses: mseoj@nus.edu.sg, ouyangjy@gmail.com (J. Ouyang).

has been reported that the graphene supporter can greatly improve the catalytic activity of Pt [35,36]. For example, Pt nanoparticles on graphene have much higher electrocatalytic activity for methanol oxidation than on carbon. Pt and bimetallic Pt alloy on graphene have been investigated as the electrocatalysts for the methanol oxidation, formic acid oxidation and oxygen reduction reactions [12,35–43]. In order to prevent the stack up of the graphene sheets, polymers were also adopted. However, metal alloy NPs on graphene have been rarely explored for the ethanol oxidation reaction (EOR). To the best of our knowledge, there is no report on investigating AuPt alloy nanocatalysts on graphene for EOR. Ethanol as a nontoxic liquid and easily available fuel has higher energy density than methanol and formic acid. But much more research work is needed for direct ethanol fuel cells as EOR is much more complicate than the oxidations of methanol and formic acid. In this study, we present a facile approach to grow AuPt alloy NPs on polyvinylpyrrolidone (PVP)-stabilized graphene. PVP can stabilize graphene in solvent, because it can be adsorbed on the surface of graphene [44]. AuPt alloy NPs on PVP-stabilized graphene (PVP-NGs-AuPt) exhibit significantly higher electrocatalytic activity than those without PVP toward EOR in alkaline media.

2. Experimental

2.1. Materials

Highly pure natural graphite powder (SP-1 graphite, purity > 99.99%) with an average particle size of $\sim 30\ \mu\text{m}$ was purchased from the Bay Carbon Inc. Other chemicals, including PVP (MW = 50,000–60,000), $\text{H}_2\text{PtCl}_6 \cdot 6\text{H}_2\text{O}$, $\text{HAuCl}_4 \cdot 3\text{H}_2\text{O}$, 5 wt% Nafion ionomer solution, 2-propanol, KMnO_4 , NaBH_4 , NaNO_3 , H_2O_2 , H_2SO_4 , NaOH , ethanol, hydrazine hydrate and HCl , were supplied by Sigma–Aldrich with the analytical grade purity. All the chemicals were used as received without any further purification.

2.2. Synthesis of PVP-stabilized graphene sheets

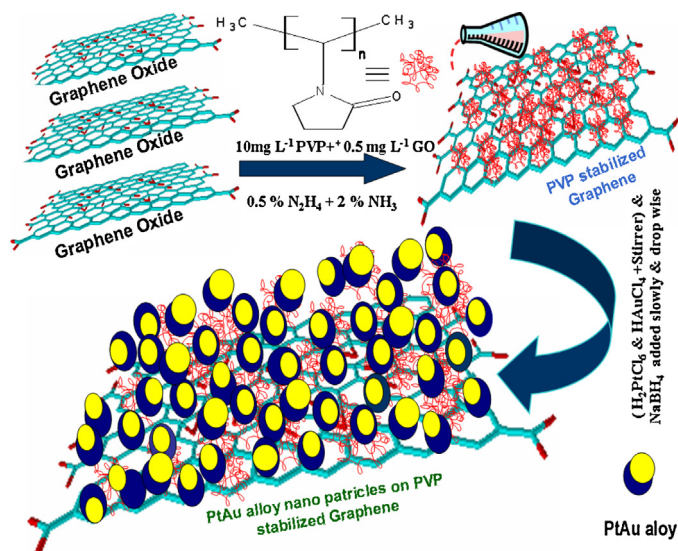
Graphene was prepared by the reduction of graphene oxide (GO). GO was synthesized according to the modified Hummer's method [45–47]. 60 mL of $10\ \text{mg mL}^{-1}$ PVP solution was mixed with 30 mL of $0.5\ \text{mg mL}^{-1}$ GO solution. The PVP/GO solution was vigorously stirred for more than 10 h. Then, 1 mL of 0.5 wt% hydrazine solution and 3 mL of 2% ammonia solution were added, and the mixture was stirred for 2 h at $100\ ^\circ\text{C}$. The black precipitate, reduced graphene oxide, was collected by vacuum filtration with 200 nm membrane filter paper. It was then washed with deionized-water for several times. Finally, the graphene sheets stabilized with PVP (NGs-PVP) were successively desiccated with a freeze-dryer for 2 days.

2.3. Growth of nanoparticles on PVP-NGs

AuPt NPs were prepared through the simultaneous reduction of $\text{H}_2\text{PtCl}_6 \cdot 6\text{H}_2\text{O}$ and $\text{HAuCl}_4 \cdot 3\text{H}_2\text{O}$ aqueous solution with NaBH_4 at the presence of an appropriate amount of NGs-PVP (Scheme 1) [48]. $\text{H}_2\text{PtCl}_6 \cdot 6\text{H}_2\text{O}$ and $\text{HAuCl}_4 \cdot 3\text{H}_2\text{O}$ had the same weight concentration in the solution. Control catalysts, Pt nanoparticles on XC-72 (C-Pt), Pt nanoparticles on graphene (NGs-Pt) and AuPt nanoparticles on XC-72 (C-AuPt), were also synthesized by the same procedure.

2.4. Materials characterization

The crystallinities of the catalysts were studied using a SEIFERT 2000 X-ray diffractometer equipped with a $\text{Cu K}\alpha$ radiation source



Scheme 1. Synthetic procedure of PVP-NGs-AuPt catalysts.

($\lambda = 0.1540\ \text{nm}$). The X-ray diffraction (XRD) patterns were identified by following the JCPDS files. The Scherrer and Bragg's formulae were used to calculate the mean diameter and the lattice parameters for each sample. Scanning electron microscopic (SEM) images were taken with a Zeiss Supra 40 FE SEM. TEM images were acquired with a HRTEM (2010F, JEOL model), which was operated at an accelerating voltage of 200 kV. Samples for TEM were prepared by suspending the catalysts on standard carbon-coated Cu grid. Energy-dispersive X-ray spectra (EDX) were obtained with a Link ISIS EDX detector coupled with the transmission electron microscope. The textural properties were analyzed by the BET method using a Quantachrome Autosorb instrument (Model AS1-CT) with nitrogen as the adsorbate [49]. The total volume (V_{tot}) and the micropore volumes (V_{m}) were derived from nitrogen sorption isotherm, and the pore size distribution was obtained according to Barrett–Joyner–Halenda (BJH) model. The X-ray photoelectron spectra (XPS) were taken using an Axis Ultra DLD X-ray photoelectron spectrometer equipped with an $\text{Al-K}\alpha$ radiation source of 150 W. The resolutions were 1 eV for XPS survey scans and 0.05 eV for the XPS fine scans. The CasaXPS software version 2.3.14 program was used to subtract the Shirley background, analyze the composition and deconvolute the XPS peaks. The survey and fine scan XPS spectra were calibrated with the $\text{sp}^2\ \text{C1s}$ band at 284.5 eV.

2.5. Electrode preparation and electrochemical studies

A catalyst ink was prepared by mixing the catalyst with 5 wt% Nafion ionomer in 2-propanol solution. It was then deposited onto the graphite block. The catalyst loading was kept at $0.40\ \text{mg cm}^{-2}$, and the geometrical surface area of the graphite block was $0.65\ \text{cm}^2$. Electrochemical measurements were conducted in a three-electrode cell using a computer-controlled Autolab 302N potentiostat/galvanostat. Ag/AgCl , a Pt foil and a catalyst were used as the reference, counter and working electrodes, respectively. The electrolyte consisting of 1 M ethanol and 0.5 M NaOH were purged with XL grade N_2 before each experiment. An ion exchange chromatography (IC) system by Metrohm's Ltd coupled with an L-7100 pump and a conductivity detector was used to analyze the reaction products during EOR. The Metrosep A Supp 5-250 and Metrosep A Supp 4-550 columns were employed to quantify the yields of acetate and carbonate ions.

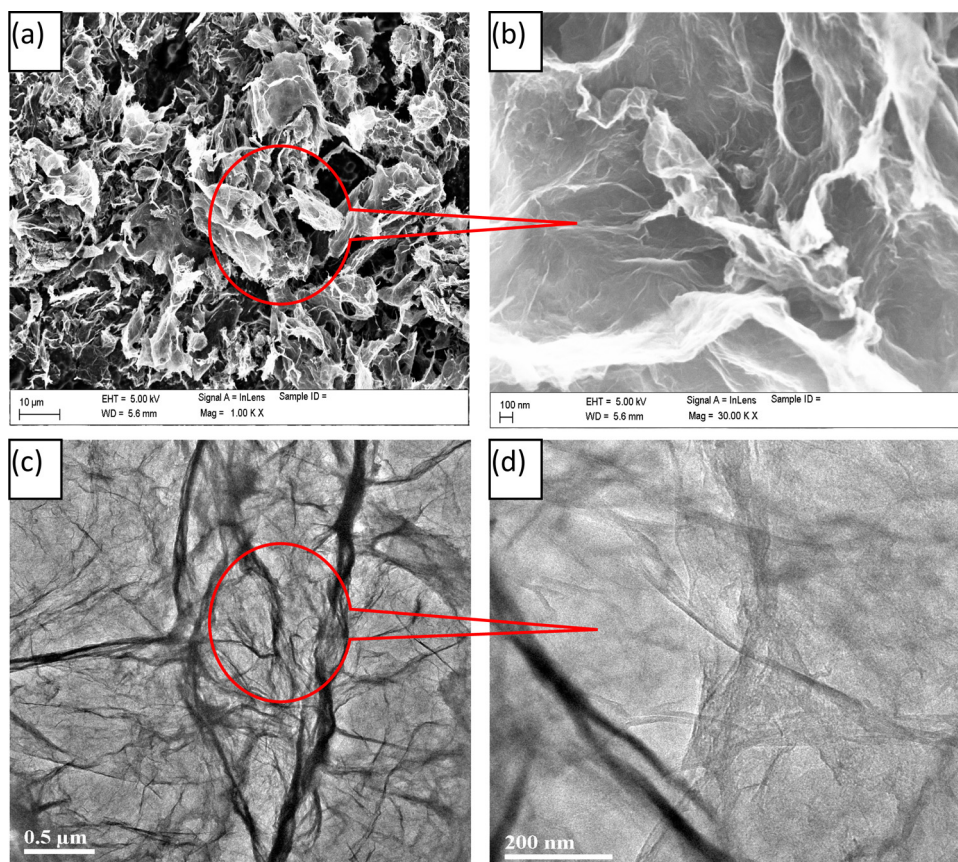


Fig. 1. (a) Low resolution and (b) high resolution SEM images, (c) low resolution and (d) high resolution TEM images of PVP-NGs.

3. Results and discussion

3.1. Physiochemical characterization of PVP-NGs-AuPt

The graphene sheets were characterized by SEM and TEM. The SEM and TEM images indicate that they have a 2D structure with a few layers (Fig. 1). The graphene sheets have a wrinkled layer structure. They overlap and connect into porous networks [50,51]. SEM and TEM analyses are also performed for PVP-NGs-AuPt and C-AuPt (Fig. 2). The AuPt NPs basically have a spherical shape. Interestingly, the alloy NPs has a better dispersion on PVP-NGs than on carbon black. The presence of PVP on the graphene surface may help prevent agglomeration of AuPt NPs [52]. The size histograms for AuPt NPs on PVP-NGs and carbon black are illustrated in Fig. 2e and f, respectively, which are based on the statistics over 300 NPs. The average particle sizes are about 3.5 nm on both supporters as listed in Table 1. The AuPt NPs were further characterized by high-resolution TEM (HRTEM) (Fig. 3a–d). The fringe pattern across the entire image indicates that the AuPt NPs are exclusively crystalline in nature. The d space of AuPt NPs on PVP-NGs calculated with the FFT analysis and also the line profile of some well-defined fringe fingerprints is 0.230 nm. It is larger than that (0.226 nm) of Pt (1 1 1) (JCPDS 04-0802). This change in the d space indicates the alloy formation of Pt and Au [49,53]. The selected area diffraction pattern (SADP) as shown in Fig. 3e indicates an *fcc* structure with good crystallinity. The concentric rings are indexed for an *fcc* crystal structure. Fig. 3f shows a representative point-resolved EDX spectrum collected from a number of individual particles, which reveals the existence of both Pt and Au. The average AuPt particle size and alloy formation were also studied by XRD (Fig. 4a). The XRD patterns of Pt and Au, the (1 1 1), (2 0 0), (2 2 0), (3 1 1) and (2 2 2) planes, are identified according to

the *fcc* crystal structures (JCPDS 04-0802 and JCPDS 04-0784). The Pt (1 1 1) peak and Au (1 1 1) patterns appear at $2\theta = 39.8$ (JCPDS 04-0802) and 38.18 (JCPDS 04-0784) for the monometallic Pt and Au, respectively. The patterns at 38.830, 45.010, 65.790, 79.230 and 82.130 degree for AuPt NPs can be assigned to (1 1 1), (2 0 0), (2 2 0), (3 1 1) and (2 2 2) of *fcc* AuPt. In comparison with the (1 1 1) pattern of Pt/C (JCPDS 04-0802) and Au/C (JCPDS 04-0784), the (1 1 1) pattern of AuPt is shifted to a lower angle by about 0.970 and higher angle by 0.650, respectively. Thus, the d spacing ($d_{111} = 0.2303$ nm) of AuPt is larger than that (2.265 Å) of pure Pt but lower than that ($d_{111} = 0.2353$ nm) of pure Au. The XRD data were fitted with the Lorentzian (Cauchy) function, and the average particle size of the NPs was calculated by the Debye–Scherrer equation [52,54]. The (1 1 1) patterns are summarized in Table 1. The particle sizes are consistent with those determined by TEM. The lattice parameter, a , for AuPt NPs is 4.0197 Å, which is larger than pure Pt ($a = 3.925$ Å) while smaller than that of pure Au ($a = 4.0813$ Å). These also confirm the alloy formation between Pt and Au [49–54].

The pore volume and pore size distributions (PSD) of the two supporters, graphene and Vulcan XC-72, were measured by the BJH nitrogen adsorption and desorption isotherm. Both supporters exhibit a typical reversible curve representative of type IV/III (Fig. S1 in supplementary information), while the supporters decorated with metal NPs have the type-III pattern (Fig. S2 in supplementary information). The hystereses of both the types are attributed to cylindrical pores. The PSD curves indicate that both micropores and mesopores region are present in both graphene and carbon supported AuPt catalysts with the pore size in the range 2–50 Å (Fig. 5). These pores can enhance the dispersion and utilization of metals. The highest adsorption peak at ~21–22 Å in the PSD curve indicates that most of PVP-NGs-AuPt can be active for the chemical reaction. In contrast, for the C-AuPt the adsorption peak is suppressed and

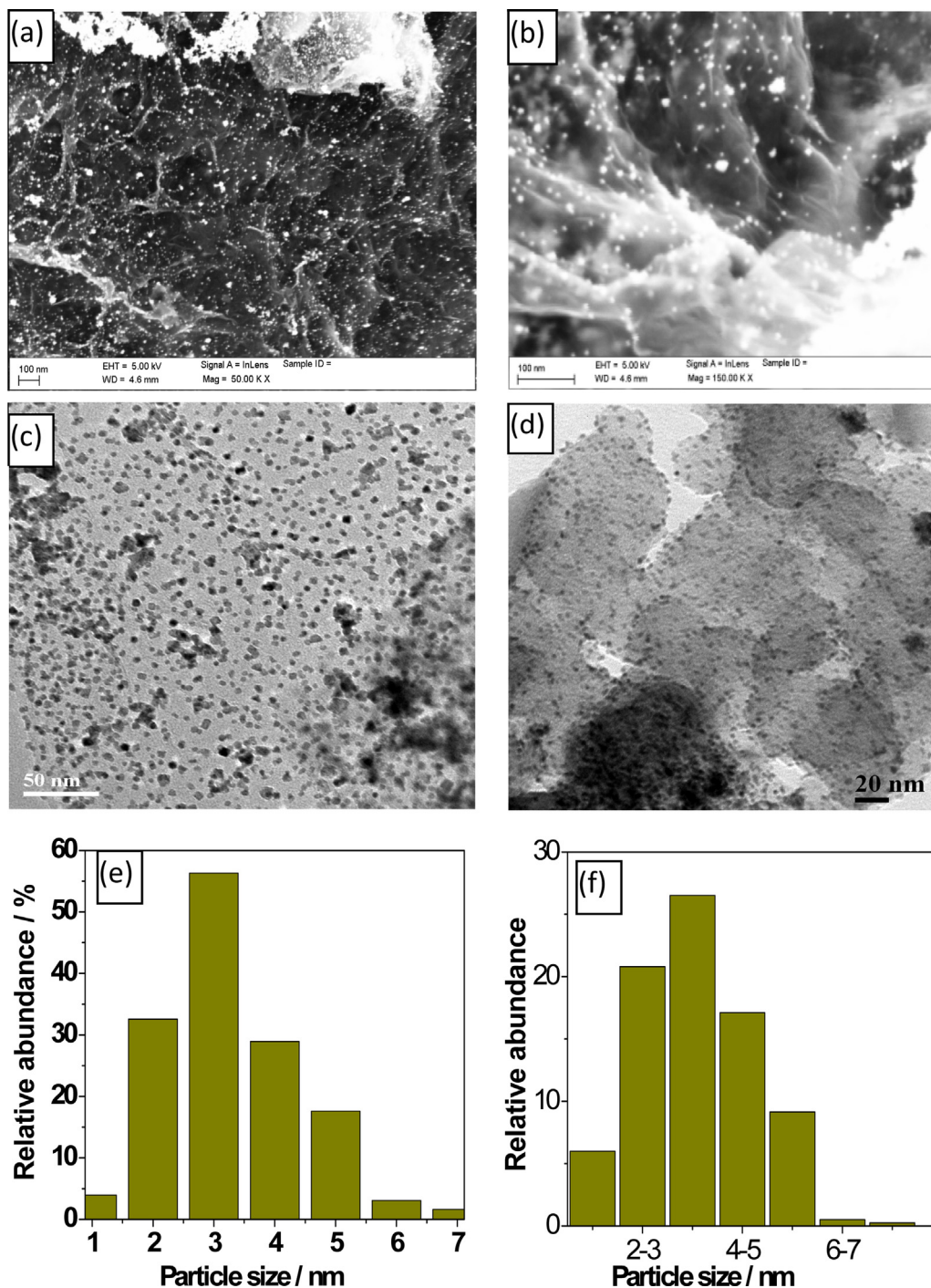


Fig. 2. SEM images of PVP-NGs-AuPt with a (a) low resolution and (b) high resolution. TEM images of (c) PVP-NGs-AuPt and (d) C-AuPt. (e and f) The AuPt particle size distributions of PVP-NGs-AuPt and C-AuPt, respectively.

Table 1

Composition, structure and characterization of catalysts as determined by EDX, XRD, TEM and voltammetric analysis of nano-catalysts.

	Average crystallite size (nm)		ECSA ($\text{m}^2 \text{g}^{-1}$)	
	XRD	TEM	H_2 ads/des region	Reduction of adsorbed O_2 -region
PVP-NGs-AuPt	3.33	3.49	78.9	77.1
NGs-AuPt	3.91	3.43	57.1	62.6
C-AuPt	3.51	3.63	43.6	51.1
NGs-Pt	3.73	3.62	33.9	39.1
C-Pt	3.83	3.53	25.1	32.3

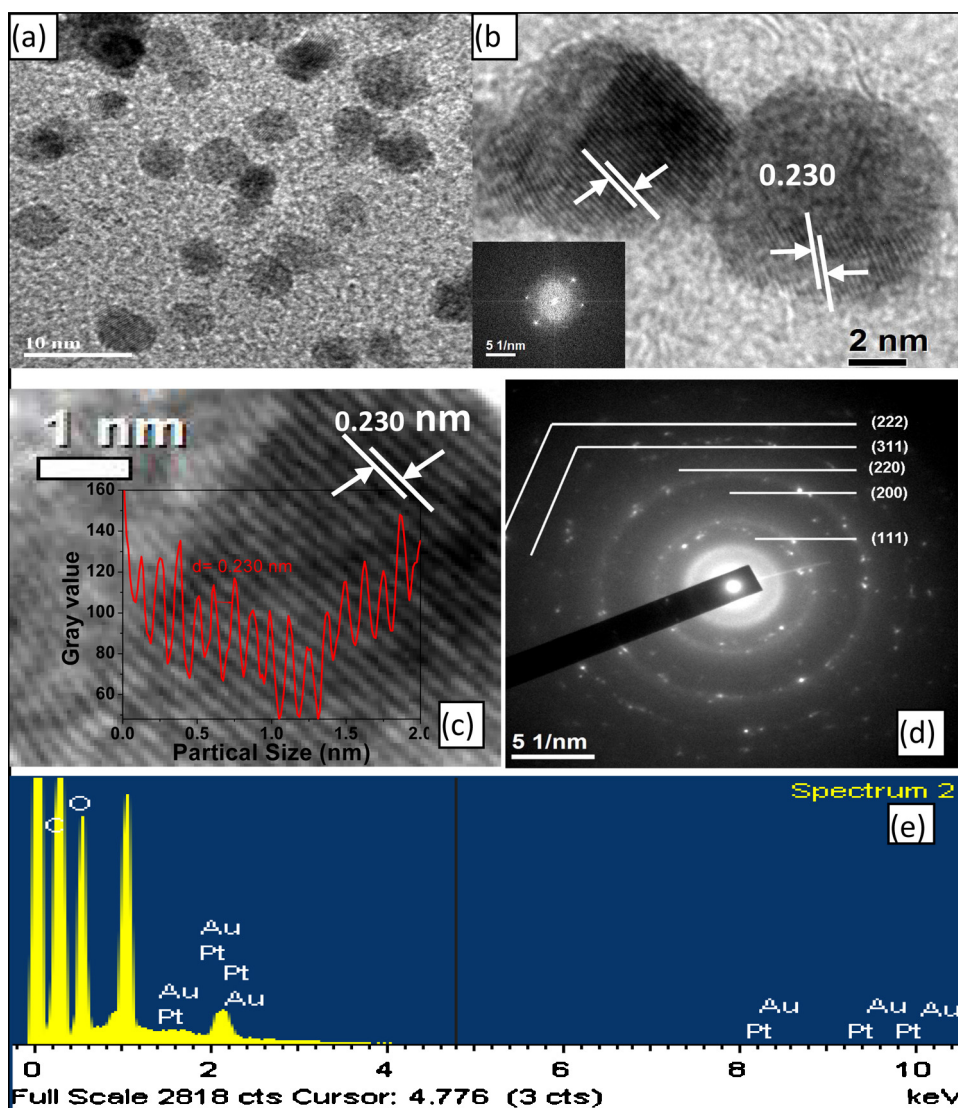


Fig. 3. (a and b) HRTEM images of AuPt NPs on PVP-NGs. The inset in (b) is FFT image of the corresponding fringe pattern. (c) Fringe pattern of a single AuPt NP. The inset is the line profile analysis of fringe fingerprints for d -spacing. (d) SADP pattern. (e) Point-resolved EDX spectrum of PVP-NGs-AuPt.

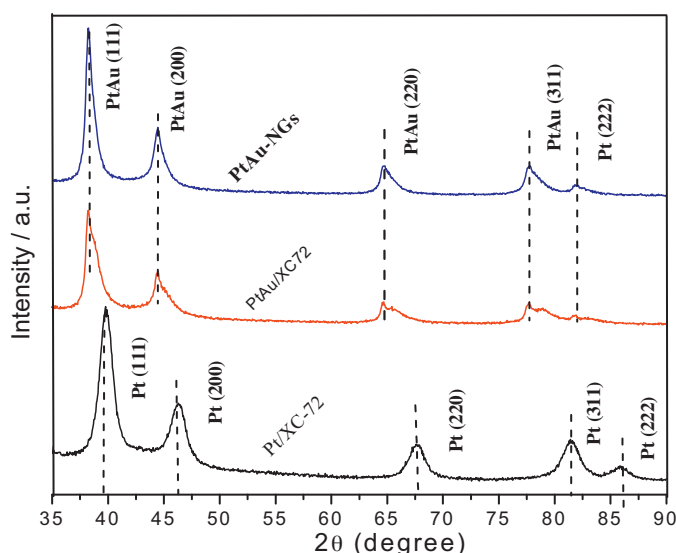


Fig. 4. XRDs of PVP-NGs-AuPt, C-AuPt and C-Pt.

there is peak broadening which extends into the mesopore regions. In terms of the isotherms (Fig. S2 in supplementary information), the total BET surface area of PVP-NGs-AuPt is $213 \text{ m}^2 \text{ g}^{-1}$, which is higher than that of NGs-AuPt ($173 \text{ m}^2 \text{ g}^{-1}$) and C-AuPt ($129 \text{ m}^2 \text{ g}^{-1}$). The large specific surface area and BET surface area (Fig. S3 in supplementary information file) suggest that PVP effectively prevents the stack up of the graphene sheets [28].

XPS was employed to identify the nature of surface species and electronic configuration of PVP-NGs-AuPt (Fig. 6). The XPS spectra of the others control samples, including PVP-NGs, Pt NPs on-PVP-C (PVP-C-Pt), Pt NPs on-PVP-graphene (PVP-NGs-Pt), C-Pt, AuPt NPs on-graphene (NGs-AuPt), AuPt NPson-C (C-AuPt), and AuPt NPs on-PVP-C (PVP-C-AuPt) are present in Fig. S4 of the supplementary information. Besides C, O, Pt and Au, N was also observed at 397 eV on the XPS survey for the samples with PVP [41,55]. The deconvolution of the C 1s XPS spectra of PVP-NGs-AuPt suggests four different C atoms, namely, non-oxygenated C at 284.6 eV, carbon in C–O at 285.6 eV, epoxy carbon at 286.7 eV, and carbonyl carbon (C=O) at 288.2 eV (Fig. S5 in supplementary information) [47,53]. Presumably, PVP chains are adsorbed on graphene surface due to the interaction between the N atoms of PVP and the conjugated C=C bonds of graphene. This interaction can modify

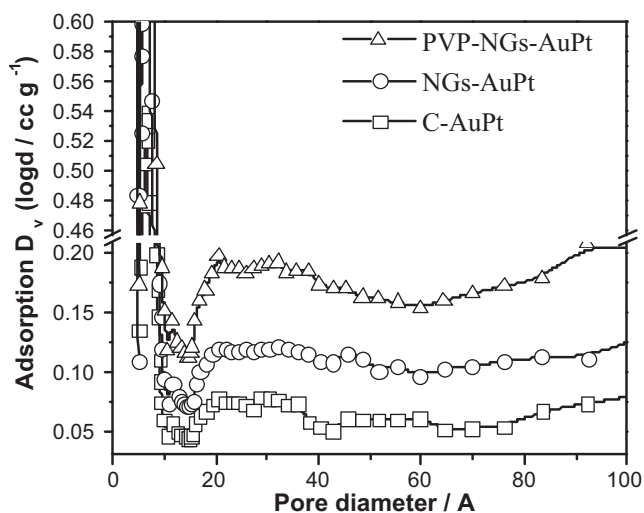


Fig. 5. Pore size distribution curve of PVP-NGs-AuPt, NGs-AuPt and C-AuPt.

the surface properties and electronic structure of graphene. This can affect the deposition of AuPt NPs on graphene and the electrocatalysis of AuPt. The deconvoluted Pt 4f XPS spectrum for the NGs-AuPt is shown in Fig. 6c. The Pt 4f_{7/2} and Pt 4f_{5/2} appear at 71.1 eV and 74.4 eV, respectively. They are assigned to the metallic Pt(0) state. The deconvolution of the Pt 4f peaks also show an additional less intense peaks at 72.1 eV and 75.4 eV for 4f_{7/2} and 4f_{5/2}, respectively. This implies the presence of a small amount of

Pt(II) or may attributed to PtO or Pt(OH)₂ [53,55]. In contrast, Au 4f_{7/2} and Au 4f_{5/2} bands appear at 84.0 and 87.7 eV, respectively, (Fig. 6d). Thus, Au is present only in the metallic state in the alloy without any surface oxide [49,53]. Interestingly, the binding energies of Pt of PVP-NGs-AuPt and PVP-C-AuPt shifted to higher energy as compared to NGs-AuPt and C-AuPt (Fig. 7a). The Au 4f binding energies are slightly higher for PVP-NGs-AuPt and PVP-C-AuPt than the monometallic Au (Fig. 7b). This can be attributed to the alloy formation of Pt and Au [49–51].

3.2. Electrocatalysis of PVP-NGs-AuPt

Fig. 8 shows the typical CVs in 0.5 M NaOH solutions with PVP-NGs-AuPt, NGs-AuPt, C-AuPt as the working electrodes, respectively. The current densities were normalized to the geometrical surface area. At least twenty cycles were performed until reproducible CVs were obtained for each of the catalysts. Hydrogen adsorption, hydrogen desorption, double layer charging, oxide formation and oxide reduction are observed on the CVs for all the three working electrodes. PVP-NGs-AuPt is featured with a wide potential span at the hydrogen adsorption–desorption region with fairly increased area, larger current output in the double layer region [56] and the high oxide reduction peak current, indicating more catalytic activity and higher electrochemical active surface area (ECSA) than NGs-AuPt and C-AuPt catalyst. The ECSAs of the PVP-NGs-AuPt, NGs-AuPt, C-AuPt were determined by measuring the charges in the hydrogen adsorption/desorption region (Q_H) after subtracting the activity arising from the double-layer charging/discharging and the coulombic charge (Q) corresponding oxide reduction peak [53]. The charges required for the reduction PtO and Au₂O₃

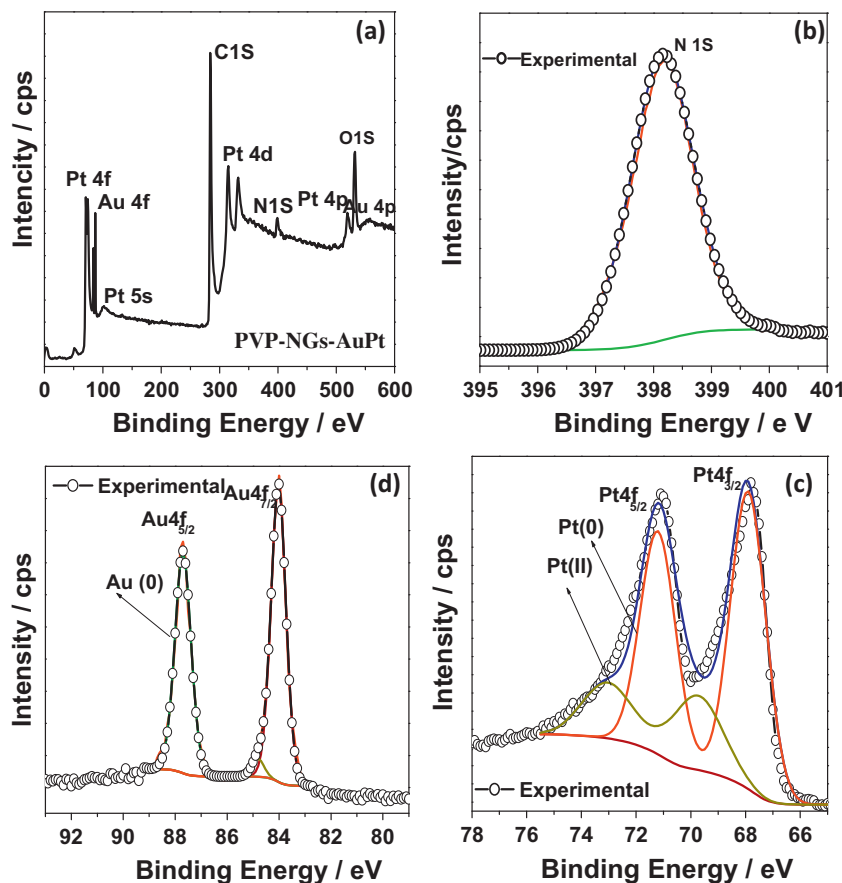


Fig. 6. (a) XPS survey spectrum of PVP-NGs-AuPt. The XPS spectra of (b) N 1S region (c) Pt 4f region (d) Au 4f region of PVP-NGs-AuPt.

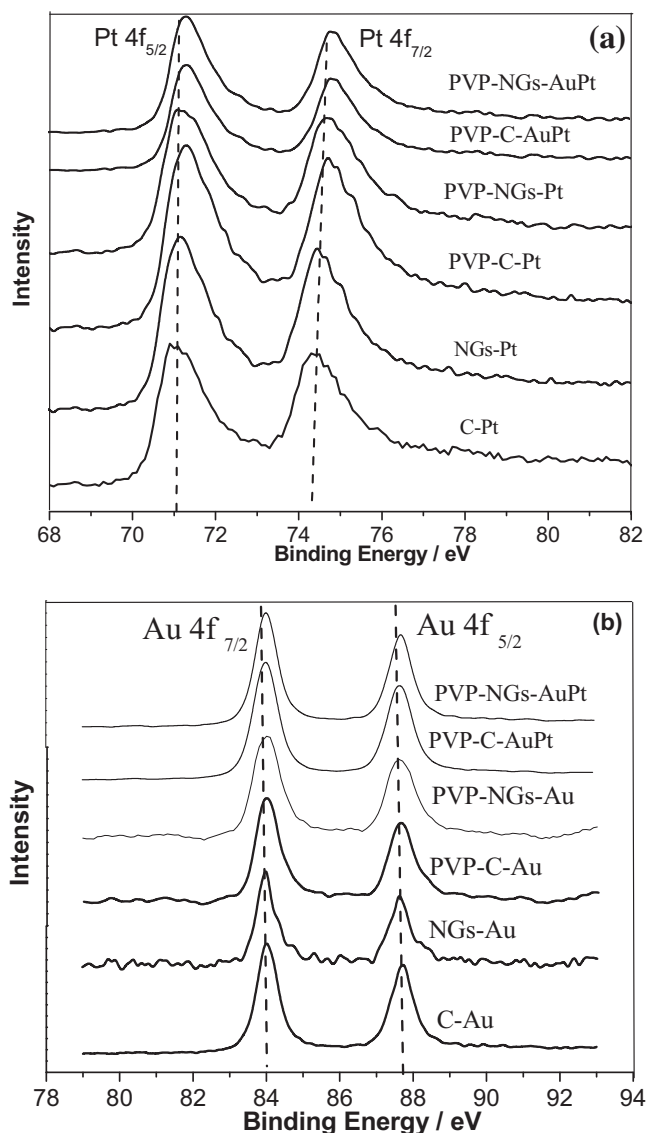


Fig. 7. XPS spectra of (a) Pt 4f region and (b) Au 4f region for different catalysts.

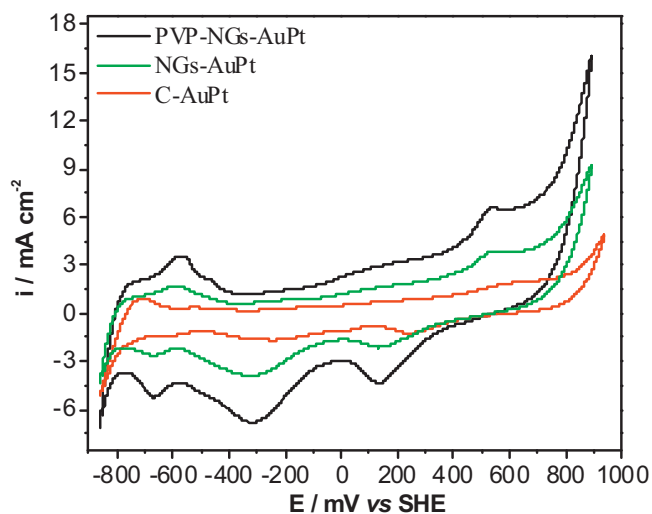


Fig. 8. Cyclic voltammograms with PVP-NGs-AuPt, NGs-AuPt and C-AuPt as the work electrodes in 0.5 M NaOH. Scan rate was 10 mV s⁻¹.

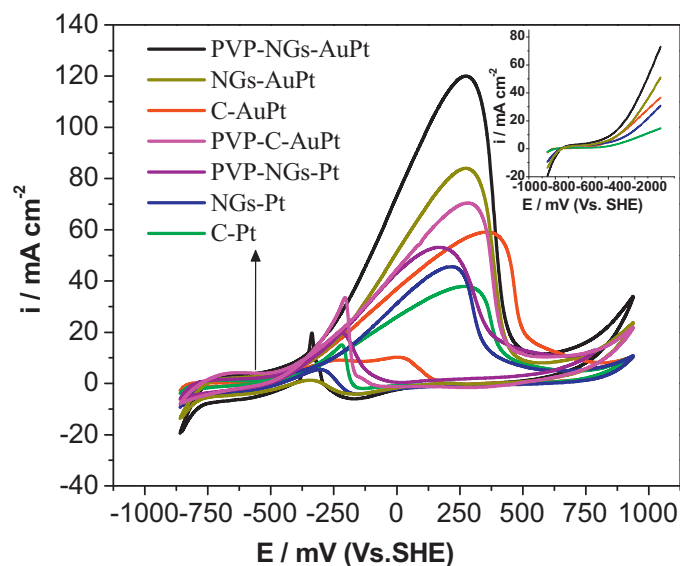


Fig. 9. Cyclic voltammograms of EOR with different working electrodes in solution of 1.0 M ethanol and 0.5 M NaOH at room temperature. The scan rate was 50 mV s⁻¹. The inset presents magnified view of onset potential region.

mono-layers were taken to be 420 and 400 $\mu\text{C cm}^{-2}$, respectively [57–59]. The mean value of charges has been taken for the oxide reduction of the PVP-NGs-AuPt, NGs-AuPt and C-AuPt with their respective atomic composition and used for evaluating the ECSA of the alloyed catalysts, summarized in Table 1.

Fig. 9 shows the CVs with PVP-NGs-AuPt, NGs-AuPt, C-AuPt, PVP-C-AuPt, PVP-NGs-Pt, NGs-Pt and C-Pt as the work electrodes in a solution of 0.5 mol L⁻¹ NaOH and 1.0 mol L⁻¹ ethanol. All the CVs have a well-defined oxidation peak in the anodic sweep and a renewed oxidation peak in the cathodic sweep. For C-Pt, EOR starts at approximately –340 mV. It shifts to negative by about 200, 330 and 450 mV for C-AuPt, NGs-AuPt and PVP-NGs-AuPt, respectively. This substantiates the higher electrocatalytic activity of the PVP-NGs-AuPt than NGs-AuPt and C-Pt and C-AuPt. Moreover, the EOR peak current density on PVP-NGs-AuPt is almost 100% and 50% higher than C-AuPt and NGs-AuPt, respectively. This also evidences the superior catalytic activity of the PVP-NGs-AuPt catalysts in comparison to the others electrocatalysts. The current density of the first peak (I_F) at potential E_F is obtained during the forward potential scan, i.e., for scanning from –860 mV to 940 mV and that of the second peak (I_B) at potential E_B is obtained in the reverse potential scan, i.e., for scanning from 940 mV to –860 mV. The potentials at which I_F values are obtained are 266 mV, 301 mV and 383 mV for PVP-NGs-AuPt, NGs-AuPt and C-AuPt, respectively. The less anodic shift of forward peak potential observed for PVP-NGs-AuPt with respect to others indicates a significant improvement in electrocatalytic activity with addition of PVP in graphene matrix. Therefore, PVP stabilized graphene is the best catalyst supporter toward EOR in alkaline medium. Moreover, E_F at lower anodic potential and E_B at higher cathodic potential of PVP-NGs-AuPt system, indicating order of time taken to remove the passivating layer formed by mainly OH and others CO poisoning species in the reverse scan. The more the dehydrogenation, the greater is the poison formation and hence greater is the time taken to remove them. The CO adsorption rate depends not only on the metal NPs but also on supporter. PVP-NGs gives rise to much smaller CO adsorption rate than graphene and carbon black at the absence of PVP [60,61].

There is strong electronic interaction between graphene and metal NPs because of the physical and chemical adsorbance and charge transfer due to their different work functions [62]. This can affect the chemical reactions on the surface of metal NPs, such as

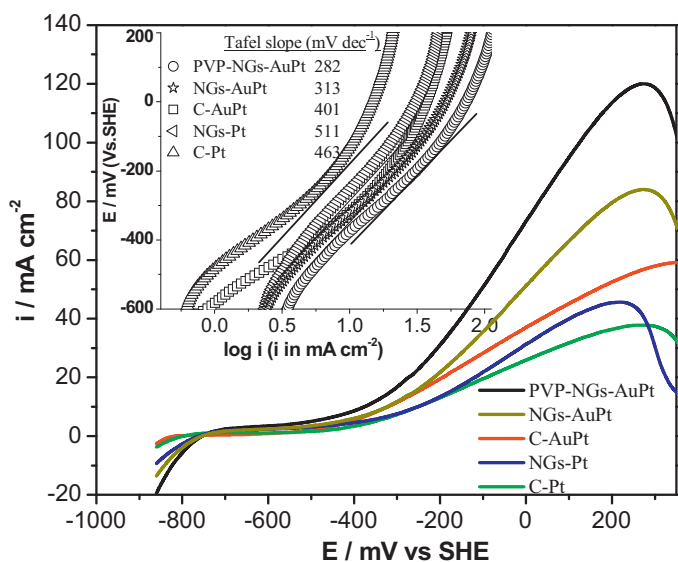


Fig. 10. Potentiodynamic polarization plots with different working electrodes in solution of 1.0 M ethanol and 0.5 M NaOH at a slow scan rate of 1 mV s⁻¹. The inset is the Tafel plots.

adsorption energies, and restrain the CO poisoning [62]. In addition, the graphene supporter can generate an extended confined space that can give rise to significant steric hindrance. It can thus prohibit the access of large species [62]. In order to obtain mass specific activity (MSA), the oxidations current density are normalized with the corresponding loading of the respective catalysts. The current density with the PVP-NGs-AuPt catalyst is almost 3 times higher than that with Pt/C, 2.45 times with NGs-Pt, 2.08 times with PVP-NGs-Pt, 1.6 times with PVP-C-AuPt and 1.35 times with NGs-AuPt (Fig. S6 in supplementary information).

Fig. 10 presents the potentiodynamic polarization plots obtained at a scan rate of 1.0 mV s⁻¹ for some catalysts. The polarization currents of the EOR on the nanocatalysts are in the order as follows: PVP-NGs-AuPt >> NGs-AuPt > C-AuPt > NGs-Pt > C-Pt at the anodic peak potential. The alloy and graphene supporter can lead to high polarization current. At the lower potential regime of lower than -500 mV, the Tafel's slopes are within 282–511 mV dec⁻¹ (inset of Fig. 10). The slope value is 282 mV dec⁻¹ at -200 mV for PVP-NGs-AuPt. It indicates faster kinetics for EOR. It is consistent with the observation that surface oxide formation at a potential less than -300 mV vs SHE on AuPt alloy catalysts. The Tafel slope increases at high potentials, signifying a change in the EOR mechanism. Presumably, the highly conductive graphene sheets stabilized with PVP play a crucial role for the polarization process by accelerating the oxidation of intermediate species during the EOR. On the other hand, the concerted effort by the alloy accounts for the catalytic superiority polymer stabilized graphene supported AuPt-NGs by OH coverage at the Au [45,49,63], assisting the dissociation of ethanol followed by the required oxygen supply for CO oxidation at Pt by the surface oxides formation of Au [49,64].

Fig. 11 shows the electrochemical impedance spectra (Nyquist plots) for EOR on C-Pt, NGs-Pt, C-AuPt, NGs-AuPt and PVP-NGs-AuPt in solution of 0.5 M NaOH and 1.0 M ethanol at -0.160 V vs SHE. The diameter of the semicircles of the Nyquist plots is due to the charge transfer resistance, R_{ct} , which is related to the EOR kinetics. The ac impedance spectra were analyzed with the equivalent circuits shown in the inset of Fig. 11. R_s and CPE represent solution resistance and the double layer capacitance, respectively. R_o and L are associated with the oxidation of the adsorbed CO. The parameters obtained by fitting the experimental results with the equivalent circuits are listed in Table 2. Both alloy and graphene

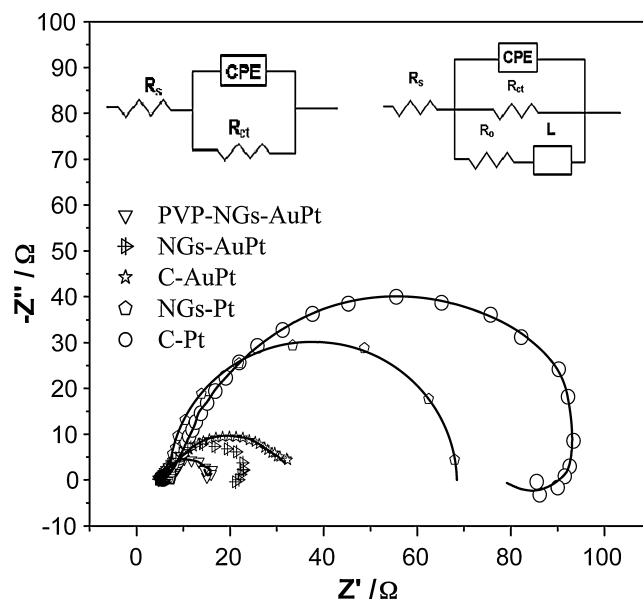


Fig. 11. Nyquist plots of EOR on PVP-NGs-AuPt, NGs-AuPt, C-AuPt, NGs-Pt and C-Pt at a -160 mV vs SHE at room temperature. The insets are the equivalent circuits.

help lower R_{ct} . PVP-NGs-AuPt exhibits the lowest R_{ct} values among the four catalysts. The R_{ct} values ally with the dissociative adsorption of ethanol in the graphene-NP interaction [65,66]. It is possibly due to the C–C bond cleavage [12,48,49]. The supporter also affects the capacitance. The capacitance of PVP-NGs-AuPt is almost double as that of C-AuPt.

Fig. 12a shows the chronoamperograms recorded at -160 mV for 1 h. The current density of PVP-NGs-AuPt is almost double as that of C-AuPt. The catalytic activities based on chronoamperometric current density are in this order: PVP-NGs-AuPt > NGs-AuPt > C-AuPt > NGs-Pt > C-Pt. PVP-NGs-AuPt has a faster EOR kinetics. PVP-NGs-AuPt shows consistently high chrono-current at the initial stage, the slight falling of polarization current and the reactivation at applied potential may be related to the early stages of adsorption of oxygenated species on AuPt-NGs. The long term poisoning rate (δ) was obtained [1,17,48,53] by measuring the linear decay of the current at times greater than 500 s on the chronoamperograms:

$$\delta = \frac{100}{i_0} \times \left(\frac{di}{dt} \right)_{t>500s} (\% s^{-1}) \quad (1)$$

where $(di/dt)_{t>500s}$ is the slope of the linear portion of the current decay and i_0 is the current at the start of polarization back extrapolated from the linear current decay [53,59,67]. As presented in Table 2, the δ value for PVP-NGs-AuPt is the lowest among these catalysts. The δ values are consistent with their poisoning tolerance indicated by voltammetry analysis. Presumably, the high conductivity of graphene and the presence of nitrogen atom of PVP may polarize the adjacent carbon atom by non-covalent π - π stacking interaction [68]. It can assist the ethanol dissociation and the CO

Table 2
Electrochemical and products analysis data for EOR on catalysts at -160 mV vs SHE.

Parameter	PVP-NGs-AuPt	NGs-AuPt	C-AuPt	NGs-Pt	C-Pt
R_{ct} (Ω)	11.21	17.31	29.7	61.8	87.3
R_s (Ω)	6.81	6.77	6.73	6.51	6.83
CPE $\times 10^{-2}$ (F cm ⁻²)	6.89	5.51	3.48	1.61	1.01
Ideality factor, n	0.88	0.93	0.81	0.98	0.92
δ (% s ⁻¹)	0.011	0.031	0.053	0.10	0.13
Acetate (mg L ⁻¹)	153	97	77.3	33.1	21.9
Carbonate (mg L ⁻¹)	243	147	110	91.7	83.1

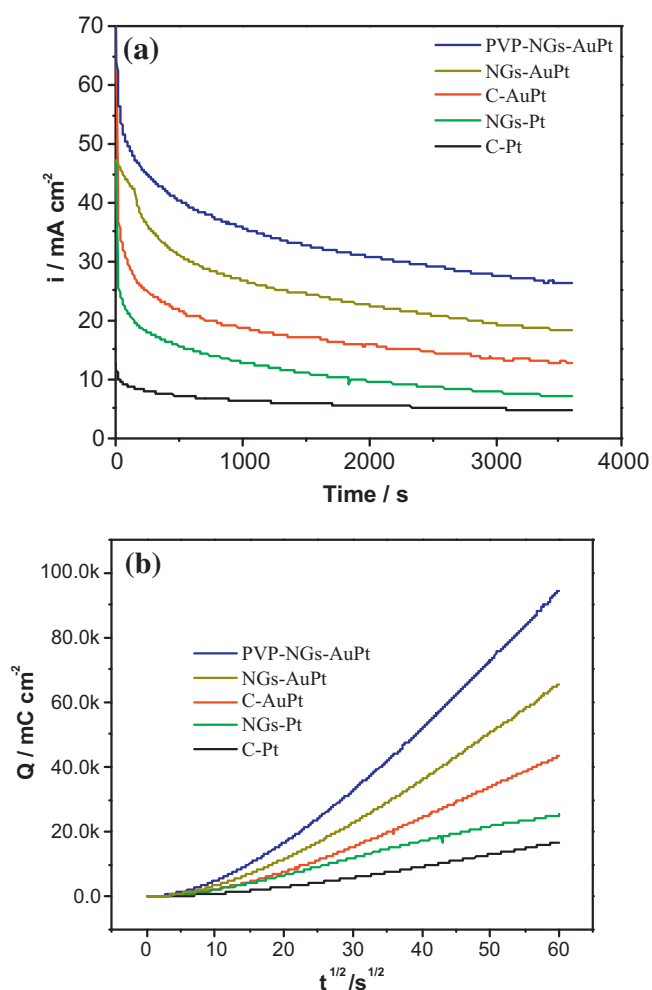


Fig. 12. (a) Chronoamperograms and (b) columbic charges charge density vs $t^{1/2}$ plots of PVP-NGs-AuPt, NGs-AuPt, C-AuPt, NGs-Pt and C-Pt obtained during the electrolysis of 0.5 M NaOH containing 1 M ethanol at -160 mV vs SHE.

diffusion. The amount of charges involved in EOR for the different electrocatalysts is determined by the Anson's plot ($Q \propto t^{1/2}$) [53,69]. As shown in Fig. 12b, the surface poisoning is much less severe for PVP-NGs-AuPt.

The δ values presents in Table 2 also suggest that AuPt Alloying can suppress the electrode poisoning. The δ values of the AuPt samples are remarkably lower than those of NGs-Pt and C-Pt. The alloying effect on poisoning is also evidenced by the results shown in Fig. 12b.

3.3. EOR products

The EOR products were analyzed by ion exchange chromatography. The ion-chromatograms are shown in Fig. 13a for acetate and Fig. 13b for the EOR products at a constant potential of -160 mV on the catalysts for a period of 1 h. The levels of acetate and carbonate become much high on the nanoparticles on PVP-NGs. The product efficiency of acetate on PVP-NGs-AuPt increases by about 98% and 58% while the carbonate formation increases by about 120% and 65% as those on C-AuPt and NGs-AuPt, respectively. The high yield of acetate and carbonate ions on PVP-NGs-AuPt electrodes also implies that the EOR follows a parallel pathway that limits the oxidation to 4e transfer processes [48,49]. This can facilitate the coverage of the catalyst surface by $(\text{OH})_{\text{ads}}$, which in turn accelerates the acetate formation. This is attributed to two facts. One is that the incorporation of Au into the Pt matrix can activate the

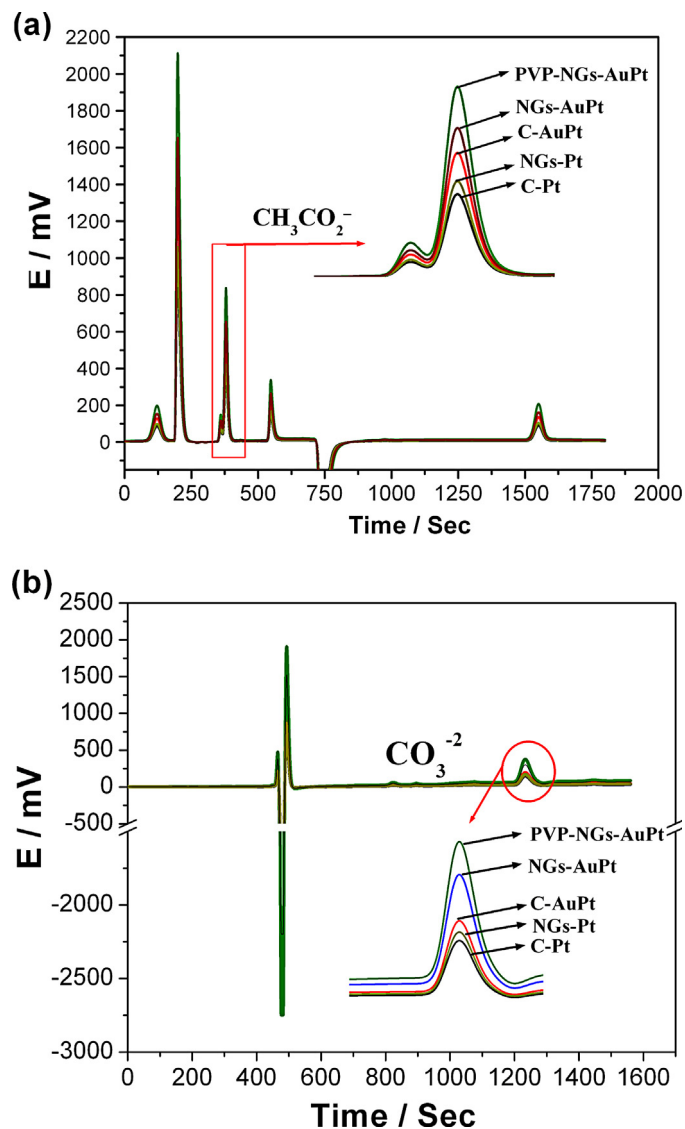


Fig. 13. Yield of acetate and carbonate estimated by ion chromatography during the electrochemical oxidation of ethanol on PVP-NGs-AuPt, NGs-AuPt, C-AuPt, NGs-Pt and C-Pt.

catalyst surface for the formation of $(\text{OH})_{\text{ads}}$ due to the image dipolar interactions [69]. The other is that the presence of PVP stabilized graphene expedites the both product yields.

4. Conclusions

PVP-NGs-AuPt sample were synthesized through the simultaneous chemical reduction of Pt and Au precursors with sodium borohydride at the presence of graphene sheets stabilized with PVP. The AuPt particle sizes are 2–5 nm as determined from XRD and TEM measurement. The surface morphology and structural of the catalysts affect the electrocatalytic activity toward EOR. PVP-NGs-AuPt shows a considerable negative shift in the onset EOR potential in comparison with C-Pt and C-AuPt. The decay in EOR current density is minimal for the PVP-NGs-AuPt, whereas Pt/C and C-AuPt show rapid current decay. The former has much higher tolerance against the poisoning species than the latter two. Moreover, PVP-NGs-AuPt reduces the charge transfer resistance and promotes the electrocatalytic activity of toward EOR. Furthermore, PVP incorporation facilitates the graphene dispersion by preventing the flocculation of graphene, and results a uniform dispersion

of AuPt NPs on graphene sheets. On the other hand, the ethanol molecule may compete with the dipolar and anion species in its ambience, to get the adsorption site on the polycrystalline catalyst surface, mostly on Pt sites during the oxidation process and at the same time, the presence of Au promote surface oxides and facilitated the surface activation by (OH)_{ads} which can activate the oxidation kinetics to a competent level of CO tolerance.

Acknowledgment

This research work is financially supported by a research grant from the Agency for Science, Technology and Research (A*STAR) in Singapore (R265-000-424-305).

Appendix A. Supplementary data

Supplementary material related to this article can be found, in the online version, at <http://dx.doi.org/10.1016/j.apcatb.2014.04.018>.

References

- [1] S. Zhang, Y.Y. Shao, G.P. Yin, Y.H. Lin, J. Mater. Chem. A 1 (2013) 4631.
- [2] S. Zhang, Y. Shao, G.P. Yin, H.Y. Lin, Angew. Chem. Int. Ed. 49 (2010) 2211.
- [3] J. Pan, C. Chen, L. Zhuang, J. Lu, Acc. Chem. Res. 45 (2012) 473.
- [4] J. Zhang, K. Sasaki, E. Sutter, R. Adzic, Science 315 (2007) 220.
- [5] N. Tian, Z.Y. Zhou, S.G. Sun, Y. Ding, Z.L. Wang, Science 316 (2007) 73.
- [6] L. Xiao, L. Zhuang, Y. Liu, J. Lu, H.D. Abruna, J. Am. Chem. Soc. 131 (2009) 602.
- [7] S. Lu, J. Pan, A. Huang, L. Zhuang, J. Lu, Proc. Natl. Acad. Sci. U. S. A. 105 (2008) 20611.
- [8] Y. Peng, C. Liu, C. Pan, L. Qiu, S. Wang, F. Yan, ACS Appl. Mater. Interface 10 (2013) 2752.
- [9] M. Haruta, Catal. Today 36 (1997) 153.
- [10] M. Vaden, X. Lai, D.W. Goodman, Science 281 (1998) 647.
- [11] C. Mihut, C. Descorme, D. Duprez, D. Amiridis, J. Catal. 212 (2002) 125.
- [12] S. Zhang, Y. Shao, H. Liao, J. Liu, I.A. Aksay, G. Yin, Y. Lin, Chem. Mater. 23 (2011) 1079.
- [13] D. Connolly, B. Twamley, B. Paullab, Chem. Commun. 46 (2010) 2109.
- [14] A. Dutta, S.S. Mahapatra, J. Datta, Int. J. Hydrogen Energy 36 (2011) 14889.
- [15] G. Yang, Y. Li, R.K. Ranab, J.J. Zhu, J. Mater. Chem. A 1 (2013) 1754.
- [16] N. Ilayaraja, N. Prabu, N. Lakshminarasimhan, P. Murugan, D. Jeyakumar, N. Ilayaraja, N. Prabu, N. Lakshminarasimhan, P. Murugan, D. Jeyakumar, J. Mater. Chem. A 1 (2013) 4048.
- [17] J.H. Choi, K.W. Park, I.S. Park, K. Kim, J.S. Lee, Y.E. Sung, J. Electrochem. Soc. 153 (2006) A1812.
- [18] Y. Kim, H.J. Kim, Y.S. Kim, S.M. Choi, M.H. Seo, W.B. Kim, J. Phys. Chem. C 116 (2012) 18093.
- [19] N.C. Cheng, H.G. Li, G.Q. Li, H.F. Lv, S.C. Mu, X.L. Sun, M. Pan, Chem. Commun. 47 (2011) 12792.
- [20] M. Carmo, V.A. Paganin, J.M. Rosolen, E.R. Gonzalez, J. Power Sources 142 (2005) 169.
- [21] R. Parsons, T. van der Noot, J. Electroanal. Chem. 257 (1988) 9.
- [22] E. Antolini, Appl. Catal. B 88 (2009) 1.
- [23] A. Balandin, S. Ghosh, W. Bao, I. Calizo, D. Teweldebrhan, F. Miao, C.N. Lau, Nano Lett. 8 (2008) 902.
- [24] A.K. Geim, K.S. Novoselov, Nat. Mater. 6 (2007) 183.
- [25] N. Tombros, C. Jozsa, M. Popinciuc, H.T. Jonkman, B.J. Wees, Nature 448 (2007) 571.
- [26] H.L. Wang, L.F. Cui, Y.A. Yang, H.S. Casalongue, J.T. Robinson, Y.Y. Liang, Y. Cui, H.J. Dai, J. Am. Chem. Soc. 132 (2010) 13978.
- [27] X. Wang, L.J. Zhi, K. Mullen, Nano Lett. 8 (2008) 323.
- [28] J. Luo, H.D. Jang, J. Huang, ACS Nano 7 (2013) 1464.
- [29] V.C. Tung, J.H. Huang, J. Kim, A.J. Smith, C.W. Chu, J. Huang, Energy Environ. Sci. 5 (2012) 7810.
- [30] V.C. Tung, J.H. Huang, I.D. Tevis, F. Kim, J. Kim, C.W. Chu, S.I. Stupp, J. Huang, J. Am. Chem. Soc. 133 (2011) 4940.
- [31] Q. Zhuo, J. Gao, M. Peng, L. Bai, J. Deng, Y. Xia, Y. Ma, J. Zhong, X. Sun, Carbon 52 (2013) 559.
- [32] Q. Zhuo, Y. Ma, J. Gao, P. Zhang, Y. Xia, Y. Tian, X. Sun, J. Zhong, X. Sun, Inorg. Chem. 52 (2013) 3141.
- [33] S.J. Cho, A. Suri, X. Mei, J. Ouyang, RSC Adv. 3 (2013) 1201.
- [34] X. Mei, H. Zheng, J. Ouyang, J. Mater. Chem. 22 (2012) 9109.
- [35] S.M. Choi, M.H. Seo, H.J. Kim, W.B. Kim, Carbon 49 (2011) 904.
- [36] Y. Xina, J.G. Liua, Y. Zhou, W. Liu, J. Gao, Y. Xie, Y. Yin, Z. Zou, J. Power Sources 196 (2011) 1012.
- [37] G. Yang, Y.J. Li, R.K. Rana, J.J. Zhu, J. Mater. Chem. A 1 (2013) 1754.
- [38] E.J. Yoo, T. Okata, T. Akita, M. Kohyama, J. Nakamura, I. Honma, Nano Lett. 9 (2009) 2255.
- [39] Y. Li, W. Gao, L. Ci, C. Wang, P.M. Ajayan, Carbon 48 (2010) 1124.
- [40] S. Guo, S. Dong, E. Wang, ACS Nano 4 (2010) 547.
- [41] S. Bong, Y.R. Kim, I. Kim, S. Woo, S. Uhm, J. Lee, H. Kim, Electrochem. Commun. 2 (2010) 1129.
- [42] L. Dong, R.R.S. Gari, Z. Li, M.M. Craig, S. Hou, Carbon 48 (2010) 781.
- [43] Q. Yue, K. Zhang, X. Chen, L. Wang, J. Zhao, J. Liu, J. Jia, Chem. Commun. 46 (2010) 3369.
- [44] A.S. Wajid, S. Das, F. Irin, H.S. Tanvir Ahmed, J.L. Shelburne, D. Parviz, R.J. Fullerton, A.F. Jankowski, R.C. Hedden, M.J. Green, Carbon 50 (2012) 526.
- [45] N.I. Kovtyukhova, P.J. Ollivier, B.R. Martin, T.E. Mallouk, S.A. Chizhik, E.V. Buzaneva, A.D. Gorchinskiy, Chem. Mater. 11 (1999) 771.
- [46] W. Hummers, R.E. Offeman, J. Am. Chem. Soc. 80 (1958) 1339.
- [47] X. Mei, J. Ouyang, Carbon 49 (2011) 5389.
- [48] A. Dutta, J. Datta, J. Phys. Chem. C 116 (2012) 2567.
- [49] J. Datta, A. Dutta, S. Mukherjee, J. Phys. Chem. C 115 (2011) 15324.
- [50] S. Stankovich, D.A. Dikin, R.D. Piner, K.A. Kohlhaas, A. Kleinhammes, Y. Jia, Carbon 45 (2007) 1558.
- [51] G. Srinivas, Y. Zhu, R. Piner, N. Skipper, M. Ellerby, R. Ruoff, Carbon 48 (2010) 630.
- [52] H. Bonnemant, W. Brijoux, R. Brinkmann, R. Fretzen, T. Jousen, R. Koppler, B. Korall, P. Neiteler, J. Richter, J. Mol. Catal. 86 (1994) 129.
- [53] A. Dutta, J. Datta, Int. J. Hydrogen Energy 38 (2013) 7789.
- [54] C.V. Rao, C.R. Cabrera, Y. Ishikawa, J. Phys. Chem. C 115 (2011) 2196348.
- [55] G. Wang, H. Wang, J. Bai, Z. Ren, J. Baic, Chem. Eng. J. 214 (2013) 386.
- [56] C.W. Xu, P.K. Shen, Chem. Commun. 2238 (2004).
- [57] S. Trasatti, O.A. Petrii, Pure Appl. Chem. 63 (1991) 711.
- [58] R.N. Singh, A. Singh, Anindita, Int. J. Hydrogen Energy 34 (2009) 2052.
- [59] J.W. Guo, T.S. Zhao, J. Prabhuram, R. Chen, C.W. Wong, J. Power Sources 156 (2006) 345.
- [60] Y. Lin, X. Cui, Langmuir 21 (2005) 11474.
- [61] E. Yoo, T. Okata, T. Akita, M. Kohyama, J. Nakamura, I. Honma, Nano Lett. 9 (2009) 2255.
- [62] P. Sutter, J.T. Sadowski, E.A. Sutter, J. Am. Chem. Soc. 132 (2010) 8175.
- [63] S.S. Mahapatra, A. Dutta, J. Datta, Electrochim. Acta 55 (2010) 9097.
- [64] E. Lee, I. Park, A. Manthiram, J. Phys. Chem. C 114 (2010) 10634.
- [65] K.J. Jeon, Z. Lee, Chem. Commun. 47 (2011) 3610.
- [66] V. Tjoa, W. Jun, V. Dravid, S. Mhaissalkarad, N. Mathews, J. Mater. Chem. 21 (2011) 15593.
- [67] Y. Liu, N. Lu, S. Poyraz, X. Wang, Y. Yu, J. Scott, J. Smith, M.J. Kim, X. Zhang, Nanoscale 5 (2013) 3872.
- [68] X.C. Qin, Z.Y. Guo, Z.M. Liu, W. Zhang, M.M. Wan, B.W. Yang, J. Photochem. Photobiol. B: Biol. 120 (2013) 156.
- [69] J. Bockris, A.K.N. Reddy, M. Aldeco, Modern Electrochemistry, vol. 2A, 2nd ed., Kluwer Academic Publisher, New York, 2002.